

# Dynamic Band-Folding Induced Giant Unconventional Anomalous Hall Effect in Magnetic Weyl Semimetal EuB<sub>6</sub>

Jianlei Shen,<sup>1,2,\*</sup> Jiacheng Gao,<sup>1,3,\*</sup> Changjiang Yi,<sup>1,\*</sup> Qingqi Zeng,<sup>1</sup> Shen Zhang,<sup>1,3</sup> Jinying Yang,<sup>1,3</sup>  
Xudan Zhang,<sup>1,3</sup> Binbin Wang,<sup>1</sup> Junzhuang Cong,<sup>1</sup> Youguo Shi,<sup>1,4</sup> Xiaohong Xu,<sup>2</sup> Zhijun Wang,<sup>1,3,†</sup>  
Enke Liu<sup>1,4,‡</sup>

<sup>1</sup>Institute of Physics, Chinese Academy of Sciences, Beijing 100190, China

<sup>2</sup>Key Laboratory of Magnetic Molecules and Magnetic Information Materials of Ministry of Education, Research  
Institute of Materials Science of Shanxi Normal University Linfen 041004, China

<sup>3</sup>School of Physical Sciences, University of Chinese Academy of Sciences, Beijing 100049, China

<sup>4</sup>Songshan Lake Materials Laboratory, Dongguan, Guangdong 523808, China

**The modulation of the electronic structure by an external magnetic field, which could further control the electronic transport behaviour of a system, is highly desired. Herein, an unconventional anomalous Hall effect (UAHE) was observed during magnetization process in the magnetic Weyl semimetal EuB<sub>6</sub>, resulting in an unconventional anomalous Hall-conductivity as high as  $\sim 1000 \Omega^{-1} \text{ cm}^{-1}$  and a Hall-angle up to  $\sim 10\%$ . The system even only shows the UAHE, meaning that the anomalous Hall signal completely comes from the UAHE, with UAHE accounting for 100% and 87.5% of the AHE and the total Hall response, respectively. Theoretical calculations revealed that a largely enhanced Berry curvature was induced by the dynamic folding of the topological bands due to the spin-canting effect under external magnetic fields, which further produced the prominent UAHE even in a low-field magnetization process. These findings elucidate the connection between the non-collinear magnetism and the topological electronic state as well as reveal a novel manner to manipulate the transport behaviour of topological electrons.**

\*These authors contributed equally to this work.

†wzj@iphy.ac.cn (Z. W.)

‡ekliu@iphy.ac.cn (E. L.)

## Introduction

In recent years, materials with topologically nontrivial electronic bands have attracted much attention due to their novel physical properties, especially for magnetic topological materials that combine magnetism and topology, such as magnetic Weyl semimetals and magnetic topological insulators, which have become one of the most advanced topics in condensed matter physics. Due to the nontrivial topological bands and time reversal symmetry breaking, magnetic topological materials exhibit diversiform, excellent transport properties, such as intrinsic anomalous Hall effect (AHE),<sup>1-6</sup> anomalous Nernst effect,<sup>7</sup> spin-orbit polarons,<sup>8</sup> and high-temperature quantum anomalous Hall effect.<sup>9</sup> As one of the most important magnetoelectric phenomenon, AHE can be intrinsically related to the Berry curvature of electronic bands.<sup>10-13</sup> In magnetic topological semimetals, gapped nodal lines and Weyl nodes near the Fermi level can produce strong Berry curvature in momentum space, which has been verified to show giant AHE in magnetic Weyl semimetal  $\text{Co}_3\text{Sn}_2\text{S}_2$  and other systems.<sup>1-6</sup> Meanwhile, the Berry curvature caused by chiral spin textures in real space often corresponds to the topological Hall effect (THE),<sup>14</sup> which is often used as the signature of skyrmions or skyrmion bubbles.<sup>15,16</sup> All these indicate that the topological properties of electronic structure and spin configuration can significantly affect the transverse transport properties of a system.

From the view of practical applications of spintronics, electronic devices and future quantum applications, it is highly desired to modulate the electronic and magnetic structures in momentum and real space, respectively, via external fields, such as temperature, pressure, electric field, and magnetic field, and further to control the electronic transport behaviors in fields. In contrast to the conventional AHE (CAHE) and the THE, recently, a nonlinear unconventional anomalous Hall effect (UAHE) was observed and attributed to the evolution of the Berry curvature in momentum space.<sup>17-20</sup> In magnetic semiconductor  $\text{EuTiO}_3$ , a nonmonotonic behavior of the AHE can be induced by the change of electronic bands due to the Zeeman splitting during magnetization process.<sup>17</sup> In the magnetic-field-induced Weyl semimetal  $\text{RPtBi}$  ( $R=\text{Gd}, \text{Dy}$ ), Weyl nodes induced by magnetic field can bring large nonlinear AHE.<sup>18,19</sup> In the canted pyrochlore ferromagnet  $\text{Nd}_2\text{Mo}_2\text{O}_7$ , the nonlinear geometrical Hall effect can be induced by mixing of electronic bands with equal or opposite spin due to spin-orbit coupling.<sup>20</sup> These phenomena indicate that the mechanism of UAHE is complex, and further researches are needed to understand the relationship

among transverse transport, electronic structure and magnetic structure, especially in emerging magnetic topological materials.

In recent years,  $\text{EuB}_6$  has been widely studied due to its interesting electronic transport properties near the FM transition temperature, such as the metal–insulator transition,<sup>21,22</sup> the giant blue shift of unscreened plasma frequencies,<sup>23,24</sup> large zero-bias anomalies,<sup>25</sup> and large negative MR.<sup>21,26</sup> However, there is yet to be a systematic study of transverse transport properties that are intrinsically related to the electronic structure of  $\text{EuB}_6$ . Recently, theoretical calculations have predicted that  $\text{EuB}_6$  is a magnetic Weyl semimetal with multiple topological states.<sup>27</sup> Topological phase transition across the Curie temperature has been further confirmed through angle-resolved photoemission spectroscopy.<sup>28,29</sup> Magnetic measurements show that there exist two types of magnetic transitions, at 15.3 and 12.5 K. The former corresponds to the disordered moments oriented along the [100] direction (Curie temperature), while the latter corresponds to the change of moments from [100] to [111] direction.<sup>30,31</sup> Notably, the theoretically calculated magnetocrystalline anisotropy energy of  $\text{EuB}_6$  is only 8 meV,<sup>27</sup> and the orientation of the magnetic moment can be easily modulated using an external magnetic field. In this case, the competition between the external magnetic field and magnetocrystalline anisotropy could potentially lead to spin-canting of the moments, which could further affect the topological and transport properties of  $\text{EuB}_6$ .

In this work, based on structural, magnetic, and transport measurements and first-principles calculations, we observed a giant UAHE due to the spin canting during the magnetization process in  $\text{EuB}_6$ . Theoretical calculations revealed that the enhanced Berry curvature, corresponding to the spin-canting effect during the magnetization process, is responsible for the UAHE. Our work demonstrates that the spin-canting effect can result in dynamic reconstruction and folding of topological bands, which can significantly affect the Berry curvature of the electronic structure and can thus affect the transverse transport properties of the materials as well.

**Basic characterizations and physical behaviours.** Single crystals of  $\text{EuB}_6$  were grown using the flux method, as shown in the inset of Fig. 1a. Room-temperature X-ray diffraction patterns of  $\text{EuB}_6$  show only the  $(h00)$  and  $(hk0)$  Bragg peaks, which indicate that the two exposed surfaces are the (100) and (110) planes, respectively, as shown in Fig. 1a. The electronic band structure of

EuB<sub>6</sub> was calculated theoretically in  $M // [100]$  without SOC [Fig. 1b]. Under the paramagnetic (PM) state at a high temperature, EuB<sub>6</sub> exhibited a semiconductor-like character with a minute direct band gap (0.02 eV).<sup>27</sup> With decreasing temperature, the magnetic state of EuB<sub>6</sub> changed from PM to FM. Meanwhile, the bands of the spin-up and spin-down channels split and moved in opposite directions. As a result, the spin-up bands crossed the Fermi level, while the gap of spin-down bands was enlarged. The band structure of EuB<sub>6</sub> in  $M // [110]$  with SOC is depicted in Fig. 1c. A pair of chiral opposite Weyl points (WP+ and WP-) can be observed in the band crossings along the P1–P2 path, which is consistent with the results of previous theoretical calculations.<sup>27</sup> These topological band structures in EuB<sub>6</sub> will significantly affect the transverse transport properties. Figure 1d shows the temperature dependence of magnetization  $M$  with the field cooling model for  $H = 0.1$  kOe along [100], [110], and [111]. Two magnetic transitions are observed during the decrease in temperature. The inset in Fig. 1d shows the temperature dependence of the  $dM/dT$  curves, in which one can see clearly that all curves exhibit two minima, at  $T_{C1}$  and  $T_{C2}$ , corresponding to the two magnetic transitions.<sup>30,31</sup>  $T_{C1}$  is 14.3 K for all directions, while  $T_{C2}$  is 11.6 K for  $H$  along [100] and 10 K for [110] and [111]. Consistent with previous reports,<sup>30,31</sup>  $T_{C1}$  corresponded to the magnetic moment along the [100] direction, while  $T_{C2}$  corresponded to the magnetic moment along the [111] direction. These results indicate that the ground state of EuB<sub>6</sub> is the magnetic moment along the [111] direction. Figure 1e shows the temperature dependence of longitudinal resistivity  $\rho_{xx}$  at 0 and 70 kOe for  $I$  and  $H$  along [001] and [100] directions, respectively. As the temperature decreased,  $\rho_{xx}$  at 0 kOe abruptly increased and then rapidly decreased, as shown in the inset in Fig. 1e. This behavior corresponds to metal–insulator transition, with the spin-up channel bands to cross through the Fermi level.<sup>27</sup> With decreasing temperature,  $\rho_{xx}$  for 70 kOe decreased and remained lower than that for 0 kOe at low temperatures, which indicates a negative  $MR$  behavior. Figure 1f shows the magnetic field dependence of  $MR$ , defined as  $MR(\%) = \frac{\rho(H) - \rho(0)}{\rho(0)}$ , at 10 K for  $I$  along the [001], [001], and [-110] directions and for  $H$  along the [100], [110], and [111]. The maximal negative  $MR$  were as high as 80%, 80%, and 86% at 50 kOe for  $H$  along [100], [110], and [111], respectively.

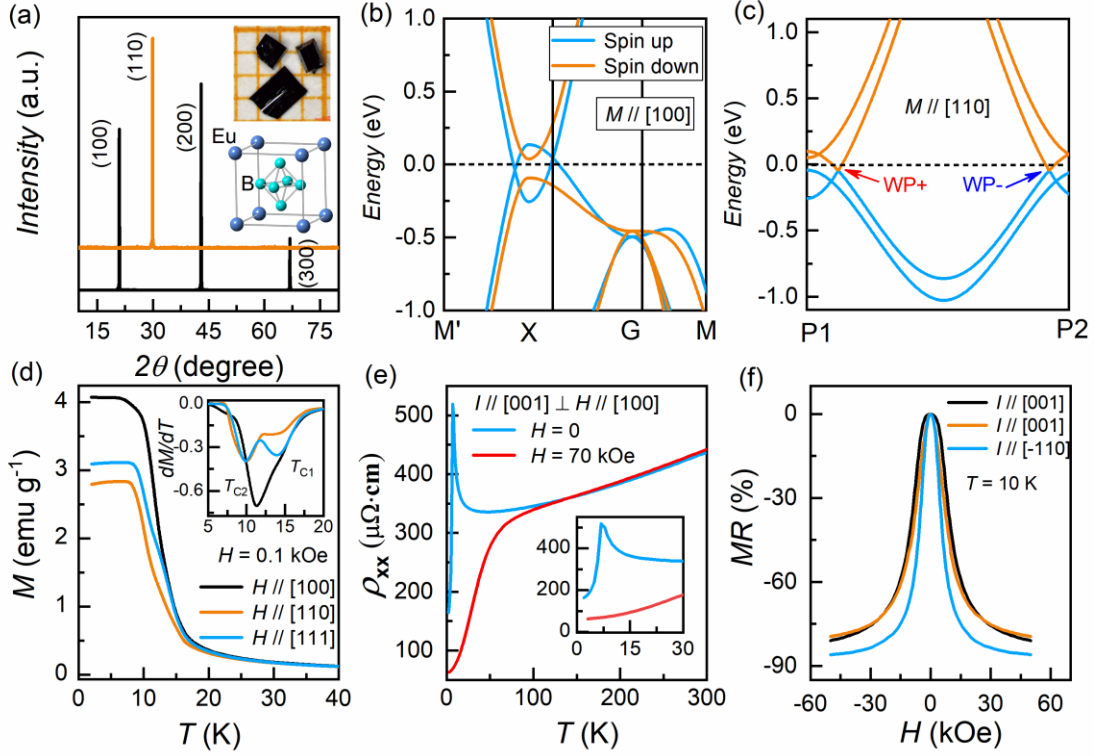


**Fig. 1 Structure, bands, magnetism and longitudinal transport of EuB<sub>6</sub>.** (a) Room temperature X-ray diffraction patterns of single crystalline samples. The insets show the crystal structure and optical morphology of single crystals. (b) Electronic band structure of EuB<sub>6</sub> in  $M // [100]$  without spin-orbit coupling (SOC). (c) Electronic band structure of EuB<sub>6</sub> in  $M // [110]$  with SOC. The band crossings around P1 and P2 are Weyl points with opposite chirality, which are denoted as WP+ and WP-, respectively. (d) Temperature dependence of magnetization  $M$  with the field cooling model for  $H = 0.1$  kOe along  $[100]$ ,  $[110]$ , and  $[111]$ . The inset shows the temperature dependence of  $dM/dT$ . (e) Temperature dependence of longitudinal resistivity  $\rho_{xx}$  at 0 and 70 kOe for  $I // [001]$  and  $H // [100]$ . The inset shows data for 2–30 K. (f) Magnetoresistance (MR) as a function of magnetic field  $H$  at 10 K for  $H$  along  $[100]$ ,  $[110]$ , and  $[111]$ .

**Unconventional anomalous Hall effect during the magnetization process.** Figures 2a, 2b, and 2c show magnetic field dependence of isothermal magnetization  $M$  (up) and Hall resistivity  $\rho_{yx}$  (down) at 2, 5, and 10 K. EuB<sub>6</sub> exhibited a saturation field  $H_S = 10$  kOe at 2 K, as shown in Fig. 2a. The saturation magnetization  $M_S$  was  $7.3 \mu_B/\text{Eu}$  at 2 K, which coincides with the full spin moment of Eu ( $4f^7$ ). In addition, the magnetization curves at 2 K for  $H$  along  $[100]$ ,  $[110]$ , and  $[111]$  exhibited very weak magnetocrystalline anisotropy, which is also consistent with the exceedingly

low magnetocrystalline anisotropy energy (8 meV) determined via prior theoretical calculations.<sup>33</sup> This finding also indicates that the magnetic moment of EuB<sub>6</sub> could be easily modulated using an external magnetic field. Below  $T_{C2}$ , the magnetic moment of the system was oriented along the [111] direction, which indicates that [111] is the easy axis. With increasing temperature, the saturation field  $H_S$  decreased and the magnetocrystalline anisotropy disappeared gradually, as shown in Figs. 2b and 2c. The dashed lines in Figs. 2a, 2b, and 2c represent the linear fit of  $\rho_{yx}$  above  $H_S$ . It can be seen that the dashed lines do not pass the original point at 2, 5, and 10 K for  $H$  along [100] and [111], which indicates the existence of CAHE. Nevertheless, the dashed lines pass through the original point at 2 and 5 K for  $H$  along [110]. This means that no CAHE existed for  $H$  along [110] at 2 and 5 K and that only a weak CAHE occurred at 10 K. It is generally accepted that  $\rho_{yx}$  is proportional to the magnetization  $M$ . However, no CAHE was observed for  $H$  along the [110] direction of EuB<sub>6</sub> under a large  $M_S$  of 7.3  $\mu_B$ /Eu. Interestingly, however, a large additional component of AHE, defined as UAHE ( $\rho_{yx}^{UA}$ ), was observed at 2 K for all directions below  $H_S$ . At 5 K,  $\rho_{yx}^{UA}$  became weaker along [110] and [100] and completely vanished along [111], leaving only the CAHE. As the temperature increased further to 10 K,  $\rho_{yx}^{UA}$  disappeared completely for all directions, and the sample exhibited only the CAHE. The UAHE cannot be interpreted as a typical CAHE in FM materials, which is usually proportional to the magnetization. Instead, the UAHE is very similar to THE, which has been observed in materials with topological spin textures in real space, such as skyrmions, in which Dzyaloshinskii–Moriya interaction (DMI) works. However, it is believed that the DMI does not exist in centrosymmetric EuB<sub>6</sub>. Therefore, the UAHE in EuB<sub>6</sub> most likely results from the evolution of the Berry curvature in the momentum space under an external magnetic field. A similar analysis was also performed in the parallel case for magnetic Weyl semimetal EuCd<sub>2</sub>As<sub>2</sub>.<sup>32</sup>

By subtracting the linear ordinary Hall term ( $R_0H$  above  $H_S$ ) from  $\rho_{yx}$  in Fig. 2a, the anomalous term  $\rho_{yx}^A$  is extracted, as shown in Fig. 2d. Unconventional and conventional AHE were detected at 2 K for  $H$  along [100] and [111], while only unconventional AHE was detected along [110] below  $H_S = 10$  kOe (also see Fig. 2a). For  $H$  along [100] and [111], the conventional

$\rho_{yx}^A$  was  $0.65 \mu\Omega \text{ cm}$  at 2 K above  $H_s$ . To obtain  $\rho_{yx}^{UA}$  below  $H_s$ ,  $\rho_{yx}^{UA}$  is defined as  $\rho_{yx}^{UA} = \rho_{yx} - \rho_{yx}^N - R_s M$ , where  $R_s$  can be determined using the data above  $H_s$  considering  $\rho_{yx}^{UA} = 0$  and  $M = M_s$  after magnetization saturation. Figure 2e shows  $\rho_{yx}^{UA}$  after subtracting the ordinary and conventional anomalous Hall terms at 2 K for  $H$  along [100], [110], and [111]. The maximum  $\rho_{yx}^{UA}$  values were 4.4, 9.6, and  $1 \mu\Omega \text{ cm}$  under  $H = 4.7, 5,$  and  $3.8 \text{ kOe}$ , respectively. Furthermore, the unconventional anomalous Hall conductivity UAHC ( $\sigma_{xy}^{UA}$ ) can be calculated via the relation  $\sigma_{xy}^{UA} = \rho_{yx}^{UA} / (\rho_{yx}^{UA2} + \rho_{xx}^2)$ . Figure 2f shows the magnetic-field dependence of  $\sigma_{xy}^{UA}$  at 2 K for the three studied axes. For  $H$  along [100], [110], and [111], the maximum  $\sigma_{xy}^{UA}$  values at 2 K were 280, 976, and  $120 \Omega^{-1} \text{ cm}^{-1}$ , respectively. In addition, the unconventional anomalous Hall angle (UAHA) at 2 K was obtained using the relation  $UAHA = \rho_{yx}^{UA} / \rho_{xx} = \sigma_{xy}^{UA} / \sigma_{xx}$ , as shown in Fig. 2g. With an increase in magnetic field, UAHA increased linearly to 4.4%, 9.6%, and 1% at 4.7, 5, and  $3.8 \text{ kOe}$  for [100], [110], and [111], respectively.

Furthermore, the UAHE only appeared during the magnetization process, i.e., before the magnetization saturation. The UAHE for [100] and [110] vanished above  $H_s = 10 \text{ kOe}$ , while that for [111] disappeared above  $7 \text{ kOe}$ . According to the magnetic measurement results, below  $T_{C2}$ , the ground state of  $\text{EuB}_6$  corresponds to the magnetic moment being oriented along [111]. When  $H$  is along [100] or [110], the spin-canting effect could arise due to the competition between the weak magnetocrystalline anisotropy and the applied magnetic field, which significantly affects the topological properties of the electronic band structure. Nevertheless, in contrast to those for [100] and [110], the UAHE for [111] disappeared promptly with increasing temperature, as shown in Figs. 2b and 2c. We attribute it to the inevitable sample tilt during the grinding process.

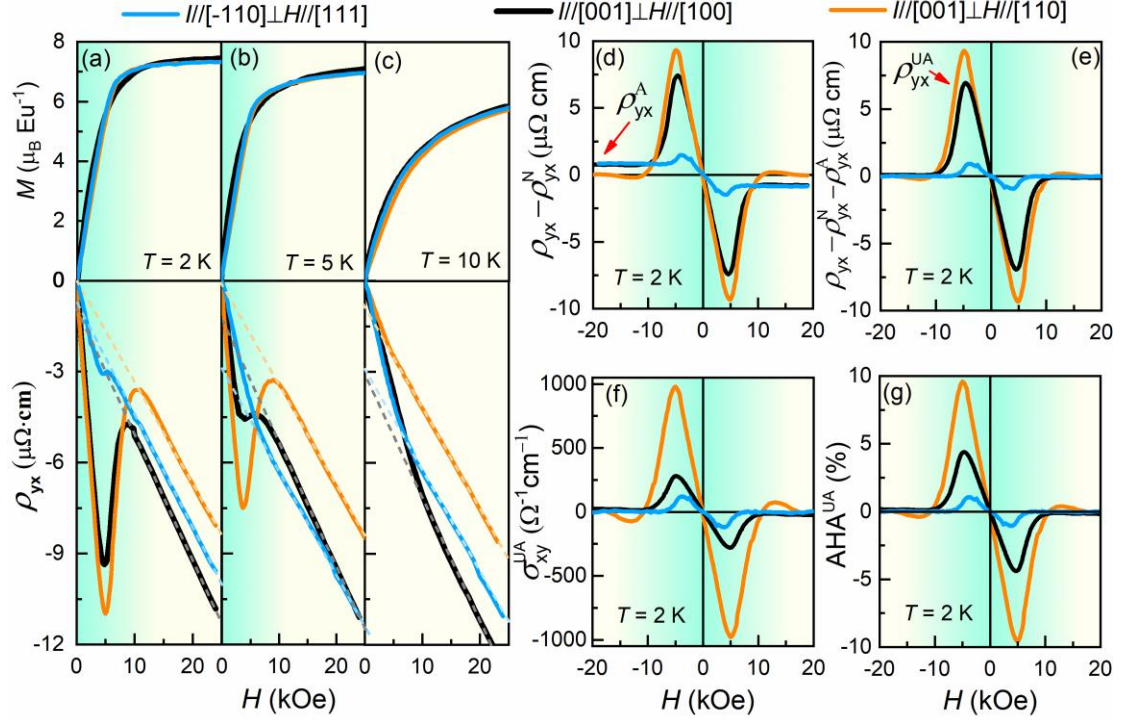


**Fig. 2 Magnetism and transverse Hall transport of EuB<sub>6</sub>.** (a), (b), (c) Magnetic field dependence of isothermal magnetization  $M$  (upper panel) and Hall resistivity  $\rho_{yx}$  (lower panel) at 2, 5, and 10 K for  $I$  along the  $[-110]$ ,  $[001]$ , and  $[001]$  and for  $H$  along  $[111]$ ,  $[100]$ , and  $[110]$ , respectively. The dashed line denotes the linear fit of the  $\rho_{yx}$  above the saturation field ( $H_s$ ). (d) Anomalous Hall resistivity  $\rho_{yx}^A = \rho_{yx} - \rho_{yx}^N$  at 2 K as a function of the magnetic field  $H$  for  $I$  along the  $[-110]$ ,  $[001]$ , and  $[001]$  and for  $H$  along  $[111]$ ,  $[100]$ , and  $[110]$ , where  $\rho_{yx}^N = R_0 H$  is the ordinary Hall term. (e) Unconventional anomalous Hall resistivity ( $\rho_{yx}^{UA} = \rho_{yx} - \rho_{yx}^N - \rho_{yx}^A$ ) at 2 K as a function of the magnetic field  $H$ . (f), (g) Unconventional anomalous Hall conductivity ( $\sigma_{xy}^{UA}$ ) and unconventional anomalous Hall angle (UAHA) at 2 K as a function of the magnetic field  $H$  for  $I$  along  $[-110]$ ,  $[001]$ , and  $[001]$  and for  $H$  along  $[111]$ ,  $[100]$ , and  $[110]$ , respectively. .

**Theoretical calculations under spin-canting configuration.** To understand the UAHE in EuB<sub>6</sub>, we performed first-principles calculations to determine the spin-canting effect on the evolution of the electronic structures. Starting from the  $z$ -directed FM order, we added the in-plane spin components ( $m_{\parallel}$ ) on different Eu atoms (marked in Fig. 3c), thus doubling the number of unit cells along all three lattice vectors. The energy difference was 8 meV when the canting angle  $\theta$  was  $45^\circ$



( $\tan\theta = m_{//}/m_z$ ); this indicates that the spin orientations can be easily tuned using external fields. Because of the band-folding effect, the band inversions appearing on the high-symmetry  $k$ -points X, Y, and Z folded to the  $\Gamma$  point. When the canted spin components became zero and the system was FM, two-fold degenerate bands existed around the  $\Gamma$  point (marked in Fig. 3a) because of the band-folding due to the equivalence of the  $x$  and  $y$  directions. Upon increasing the canted spin components, the degenerated bands split, and all crossings along  $\Gamma$ -Z became gapped due to SOC. Although the energy scale of the spin-canting-induced band splitting was small (less than 20 meV on the  $\Gamma$  point), the bands changed considerably upon being coupled with the previous singly-degenerate band (green regions in Figs. 3d and 3e), leading to an enhancement in the Berry curvature on the coupled area.

The Berry curvature can be calculated directly using the linear-response Kubo formula. We calculated the Berry curvature  $\Omega_{xy}$  along the high-symmetry  $\Gamma$ -Z line, on which  $\Omega_{yz}$  and  $\Omega_{zx}$  always have the same value due to the  $\Theta m_{-110}$  symmetry. Each peak on the Berry curvature spectrum corresponds to the band-crossing regime on the band structure. When the canting angle is zero, the bands arising from the high-symmetry  $k$ -points X and Y (doubly degenerate bands) do not couple with the bands from the Z point (single degenerate band). Due to the spin-canting effect, these bands couple and open gaps, which induce two additional peaks on the Berry curvature spectrum (the two peaks on the left in Fig. 3g). When  $H$  is smaller than  $H_S$ , the electronic band structure can be efficiently modulated by this behavior of the non-collinear magnetism. The folding of electronic band structure results in the UAHE in the magnetization process. However, when  $H$  is larger than  $H_S$ , all magnetic moments follow the direction of the external magnetic field, and both the spin-canting effect and UAHE disappear, leaving only the CAHE due to the collinear ferromagnetism with the spin-orbit coupling. Furthermore, when  $H$  exceeds  $H_S$  at 2 K, the conventional AHC is only 24 and 85  $\Omega^{-1} \text{ cm}^{-1}$  for [100] and [111], respectively, which is consistent with the results of theoretical calculations for the collinear FM state.<sup>27</sup>

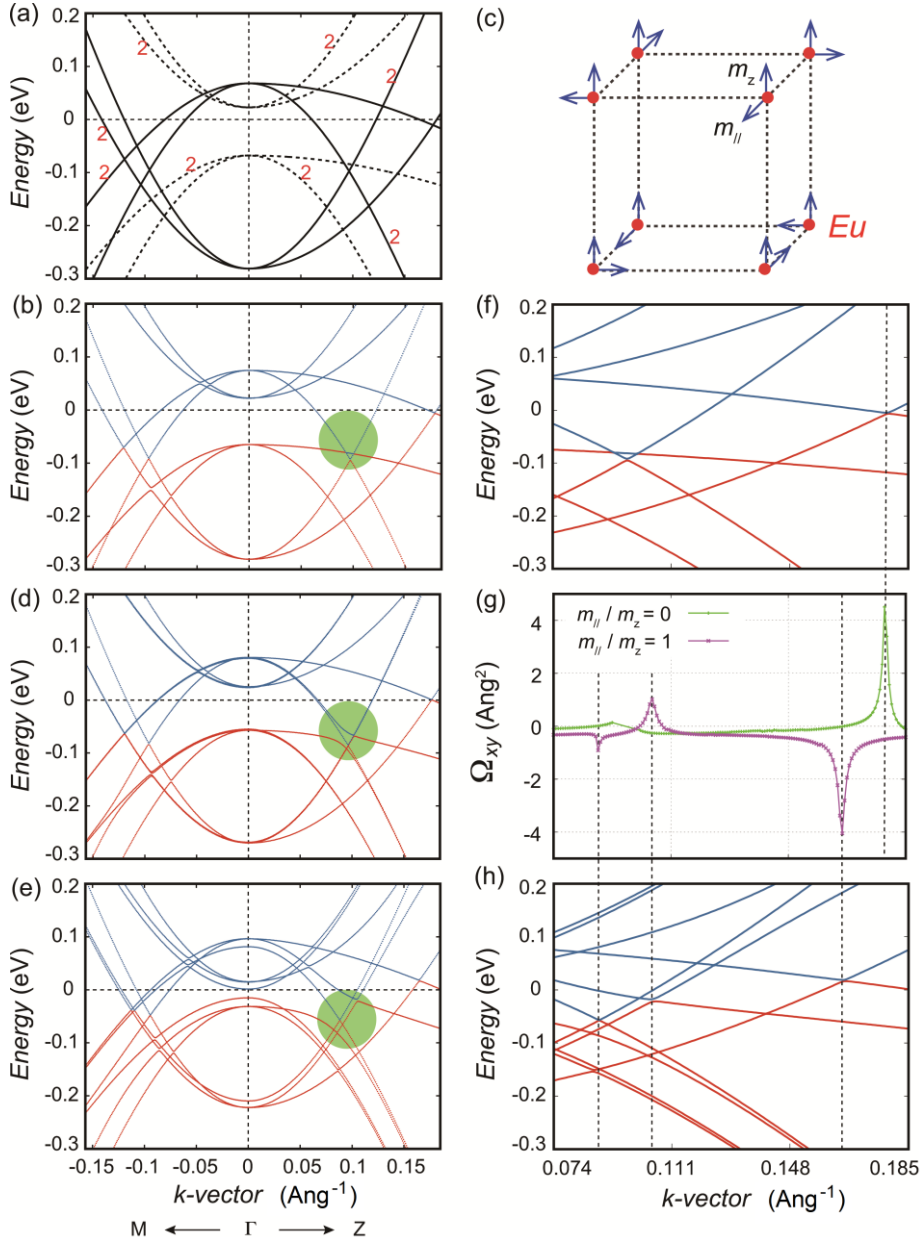


**Fig. 3 Band structure and Berry curvature with spin-canting effect.** (a) FM-order band structure for enlarged supercell without considering SOC. The doubly degenerate bands are marked specifically. (b) FM-order bands after considering SOC. (c) Schematic of magnetic orientation on each Eu atom in the supercell. (d), (e) Spin-canting band structures with different in-plane magnetic moments for canting angle  $\theta = 15^\circ$  and  $45^\circ$ , respectively. (f), (h) Band-crossing regime for  $\theta = 0^\circ$  and  $45^\circ$  on  $\Gamma$ -Z. (g) Calculated Berry curvature  $\Omega_{xy}$  around the band-crossing regime on  $\Gamma$ -Z.

**Modulation of electronic band structure and transverse electron transport behaviors.** In order to provide a clear physics picture, the schematic diagram of the modulation of electronic band structure and transverse electron transport characteristics was depicted in Fig. 4 for  $H$  along

[111], [100], and [110] directions of magnetic Weyl semimetal  $\text{EuB}_6$  during the whole magnetization process. According to the magnetic measurement results in Fig. 1d, the groundstate magnetic moment of  $\text{EuB}_6$  align with [111] direction at  $2 \text{ K} < T_{C2}$ , which means that [111] direction is the easy axis (Figs. 4a and 4b). For  $H$  along easy axis [111], there is no spin-canting and band-folding effects during the whole magnetization process, so it only shows the CAHE due to the original topological bands, as shown in the upper part of Figs. 4b-d. When the moment deviates from the easy axis to the hard axis during magnetization process, the competition between the magnetocrystalline anisotropy and external magnetic field will lead to spin canting in real space. The moment rotation driven by external field will lead to a resultant band-folding effect in momentum space, which leads to splitting of original band and producing additional bands, as shown in red color in the middle and bottom of Fig. 4c. With the aid of the split bands and anti-crossings due to SOC, the enhancement in the Berry curvature can be obtained. For the case of magnetization saturation, all moments follow the direction of the external magnetic field, and both the spin canting and band folding disappear, as shown in the middle and bottom of Fig. 4d. For  $H$  along [100] and [110] directions, an enhancement in the Berry curvature induced by spin-canting and band-folding effects leads to UAHE during the magnetization process. The spin-canting, band-folding, as well as the UAHE will disappear at the same time except the CAHE, once the system enters the states of magnetization saturation along the main crystal axes, as shown in Figs. 4d and 4e. It is worth noting that there is also very small UAHE for  $H$  along [111] at 2 K in Fig. 2, which is attributed to the inevitable sample tilt during the grinding process. It implies that as long as the magnetic field deviates from the easy axis [111] direction, it is very likely to see a dynamic picture of spin-canting, band-folding, and UAHE before the saturation magnetization in the present system.

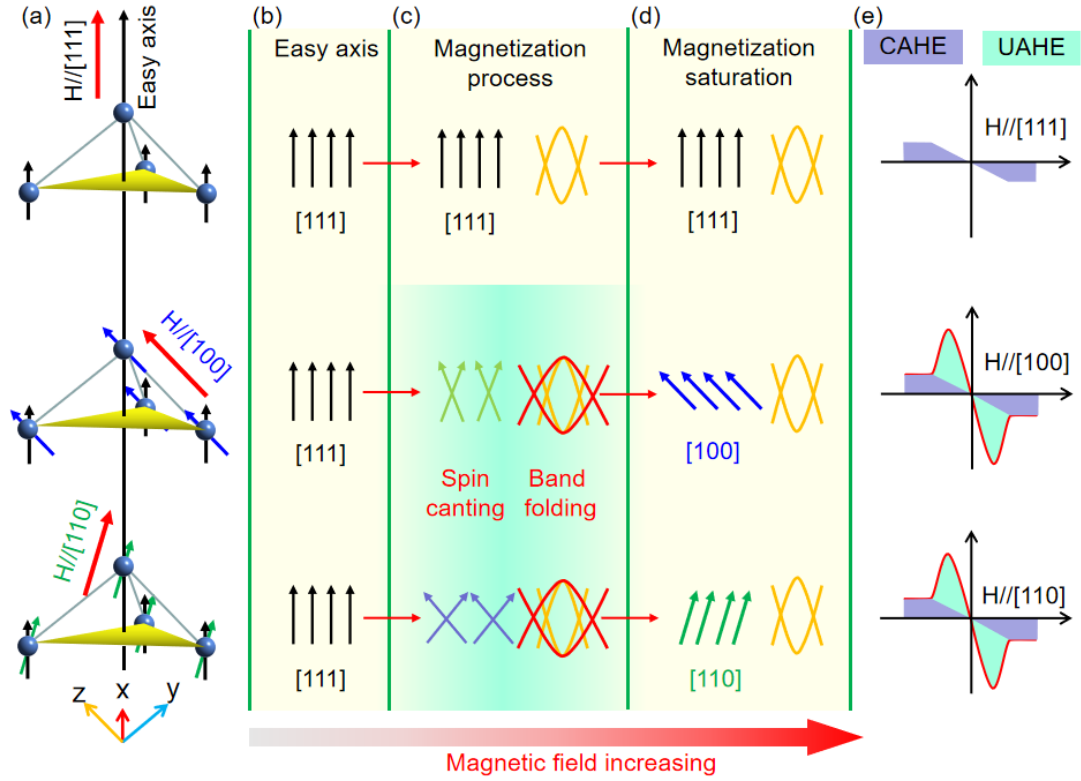


**Fig. 4 Schematic diagram of the modulation of electronic band structure and transverse electron transport characteristics.** (a) Magnetic fields along [111], [100], and [110] directions and the rotations of the magnetic moments. (b) Magnetic moment along easy axis [111] direction in the ground state below  $T_{C2}$ . (c) Spin-canting and band-folding effects in low-field magnetization process for  $H$  along [100] and [110], respectively. There is no spin-canting and band-folding effects for  $H$  along easy axis [111]. (d) Magnetic moments along the external magnetic field and electronic bands for saturated magnetization. Spin-canting and band-folding effects disappear again in this case. (e) CAHE and UAHE for  $H$  along different crystal axes. The red arrow at the bottom indicates the direction of the increasing magnetic field.

**Comparison of UAHE.** At present, the reported systems with UAHE induced by modulation of the electronic structure via external magnetic field are very rare. If we compared to previously reported results for the UAHE of the typical materials, the UAHC ( $\sim 1000 \Omega^{-1} \text{ cm}^{-1}$ ) and UAHA ( $\sim 10\%$ ) of  $\text{EuB}_6$  are seen to be larger than those of these materials, as shown in Fig. 5a. It is worth noting that the UAHE of  $\text{GdPtBi}$  and  $\text{DyPtBi}$  are very prominent, but both of them correspond to higher magnetic fields.<sup>18,19</sup> The UAHE is mainly attributed to the evolution of energy bands induced by a magnetic field. Therefore, the comparison between UAHC and UAHA produced in a

unit magnetic field is more meaningful. Figure 5b shows UAHC and UAHA produced in a unit magnetic field for the UAHE of the typical materials, where  $H_{\max}$  corresponds to the largest UAHC and UAHA in these materials. Due to the larger UAHC of  $\text{EuB}_6$  in the lower magnetic field, UAHC of unit magnetic field is the largest in these materials. It also indicates that the magnetic structure in  $\text{EuB}_6$  is easily controlled by the lower magnetic fields, which can significantly affect the electronic structure and the macroscopic transport properties. When  $H$  is along [110] direction,  $\text{EuB}_6$  only shows a giant UAHE, and there is no CAHE, which means that the anomalous Hall signal in  $\text{EuB}_6$  completely comes from the UAHE induced by modulation of the electronic structure via the external magnetic field. That is to say, UAHE accounts for 100% of the total AHE, while UAHE accounts for 87.5% of the total Hall response, which includes normal Hall effect, CAHE, and UAHE, as shown in Fig. 5c.

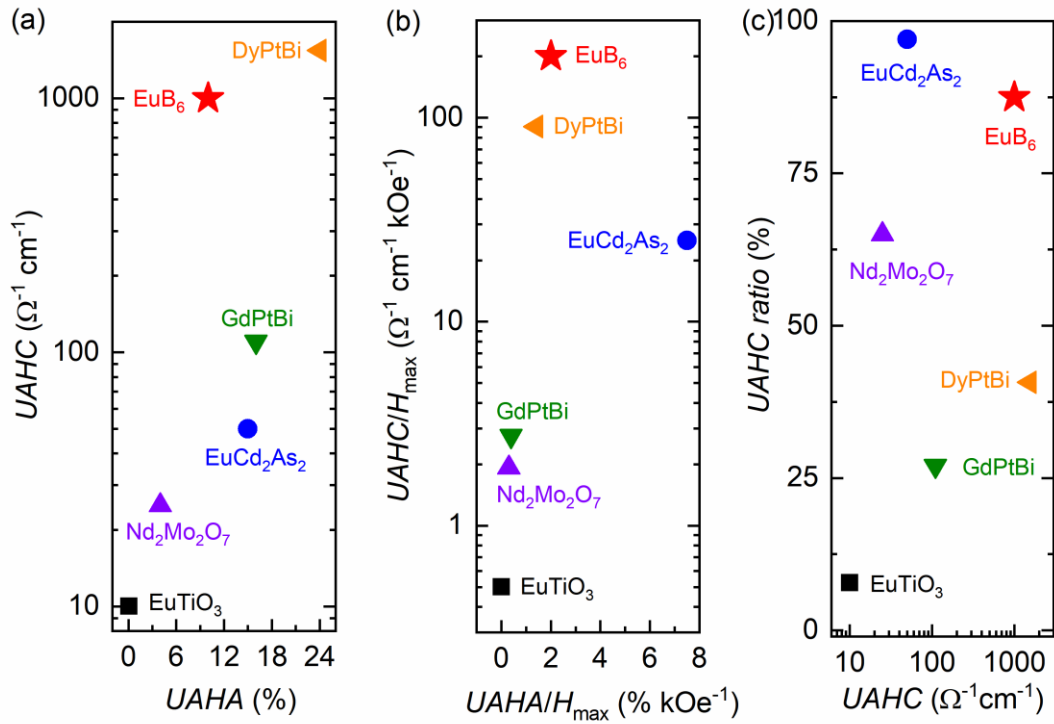


**Fig. 5 Comparison of UAHE between our work and reported materials.** (a), (b), (c) Comparison of unconventional anomalous Hall conductivity (UAHC) and unconventional Hall angle (UAHA), UAHC and UAHA per magnetic field, and UAHC ratio in our work and typical materials ( $\text{EuTiO}_3$ ,<sup>17</sup>  $\text{Nd}_2\text{Mo}_2\text{O}_7$ ,<sup>20</sup>  $\text{EuCd}_2\text{As}_2$ ,<sup>32</sup>  $\text{GdPtBi}$ ,<sup>18</sup> and  $\text{DyPtBi}$ <sup>19</sup>) with modulation of the electronic structure via external magnetic field.

In conclusion, based on structural, magnetic, and transport measurements and first-principles calculations, a giant UAHE was observed in magnetic Weyl semimetal  $\text{EuB}_6$  during the magnetization process along a hard axis; a maximum UAHC of  $\sim 1000 \text{ } \Omega^{-1} \text{ cm}^{-1}$  and UAHA of  $\sim 10\%$  were found for the  $I // [001]$  direction and  $H // [110]$ , contributing unprecedentedly 87.5% of the total Hall response. Theoretical calculations revealed that the Berry curvature was enhanced by the dynamic reconstruction and folding of topological bands due to the spin-canting effect during the magnetization, which is driven by the competition between the magnetocrystalline anisotropy and external magnetic field; this resulted in the UAHE. Our findings provide not only insight into the relation between magnetic structure and electronic structure but also effective guidance for manipulating the transverse electric and thermal transport properties via external magnetic field, especially in emergent magnetic topological materials.

## References

1. Liu, E. K. et al. Giant anomalous Hall effect in a ferromagnetic Kagome-lattice semimetal, *Nat. Phys.* **14**, 1125-1131 (2018).
2. Wang, Q. et al. Large intrinsic anomalous Hall effect in half-metallic ferromagnet  $\text{Co}_3\text{Sn}_2\text{S}_2$  with magnetic Weyl fermions. *Nat. Commun.* **9**, 3681 (2018).
3. Shen, J. L. et al. Local Disorder-Induced Elevation of Intrinsic Anomalous Hall Conductance in an Electron-Doped Magnetic Weyl Semimetal. *Phys. Rev. Lett.* **125**, 086602 (2020).
4. Belopolski, I. et al. Discovery of topological Weyl fermion lines and drumhead surface states in a room temperature magnet. *Science* **365**, 1278 (2019).
5. Li, P. et al. Giant room temperature anomalous Hall effect and tunable topology in a ferromagnetic topological semimetal  $\text{Co}_2\text{MnAl}$ . *Nat. Commun.* **11**, 3476 (2020).
6. Kim, K. et al. Large anomalous Hall current induced by topological nodal lines in a ferromagnetic van der Waals semimetal. *Nat. Mater.* **17**, 794-799 (2018).
7. Guin, S. N. et al. Zero-Field Nernst Effect in a Ferromagnetic Kagome-Lattice Weyl-Semimetal  $\text{Co}_3\text{Sn}_2\text{S}_2$ . *Adv. Mater.* **31**, e1806622 (2019).
8. Xing, Y. Q. et al. Localized spin-orbit polaron in magnetic Weyl semimetal  $\text{Co}_3\text{Sn}_2\text{S}_2$ . *Nat. Commun.* **11**, 5613 (2020).
9. Deng, Y. J. et al. Quantum anomalous Hall effect in intrinsic magnetic topological insulator  $\text{MnBi}_2\text{Te}_4$ . *Science*, **367**, 895 (2020).
10. Karplus, K. et al. Hall effect in ferromagnetics. *Phys. Rev.* **95**, 1154-1160 (1954).
11. Sundaram, G. et al. Wave-packet dynamics in slowly perturbed crystals: Gradient corrections and Berry-phase effects. *Phys. Rev. B* **59**, 14915-14925 (1999).
12. Jungwirth, T. et al. Anomalous Hall effect in ferromagnetic semiconductors. *Phys. Rev. Lett.* **88**, 207208 (2002).
13. Onoda, M. et al. Topological nature of anomalous Hall effect in ferromagnets. *J. Phys. Soc. Jap.* **71**, 19-22 (2002).
14. Hou, Z. P. et al. Observation of Various and Spontaneous Magnetic Skyrmionic Bubbles at Room Temperature in a Frustrated Kagome Magnet with Uniaxial Magnetic Anisotropy. *Adv. Mater.* **29**, 1701144 (2017).
15. Wang, Q. et al. Anomalous Hall effect in a ferromagnetic  $\text{Fe}_3\text{Sn}_2$  single crystal with a geometrically frustrated Fe bilayer kagome lattice. *Phys. Rev. B* **94**, 075135 (2016).
16. Wang, Q. et al. Anomalous Hall effect in a ferromagnetic  $\text{Fe}_3\text{Sn}_2$  single crystal with a geometrically frustrated Fe bilayer kagome lattice. *Phys. Rev. B* **94**, 075135 (2016).
17. Takahashi, K. S. et al. Anomalous Hall effect derived from multiple Weyl nodes in high-mobility  $\text{EuTiO}_3$  films. *Sci. Adv.* **4**, eaar7880 (2018).
18. Suzuki, T. et al. Large anomalous Hall effect in a half-Heusler antiferromagnet. *Nat. Phys.* **12**, 1119-1123 (2016).
19. Zhang, H. et al. Field-induced magnetic phase transitions and the resultant giant anomalous Hall effect in the antiferromagnetic half-Heusler compound  $\text{DyPtBi}$ . *Phys. Rev. B* **102**, 094424 (2020).
20. Hirschberger, M. et al. Geometrical Hall effect and momentum-space Berry curvature from spin-reversed band pairs. *Phys. Rev. B* **103**, L041111 (2021).
21. Guy, C. et al. Charge transport and pressure dependence of  $T_c$  of single crystal, ferromagnetic

- EuB<sub>6</sub>. Solid State Commun. **33**, 1055 (1980).
22. Nyhus, P. et al. Spectroscopic study of bound magnetic polaron formation and the metal-semiconductor transition in EuB<sub>6</sub>. Phys. Rev. B **56**, 2717 (1997).
  23. Degiorgi, L. et al. Low-Temperature Anomalies and Ferromagnetism of EuB<sub>6</sub>. Phys. Rev. Lett. **79**, 5134 (1997).
  24. Broderick, S. et al. Scaling between magnetization and Drude weight in EuB<sub>6</sub>. Phys. Rev. B **65**, 121102(R) (2002).
  25. Amsler, B. et al. Electron-tunneling studies of the hexaboride materials SmB<sub>6</sub>, EuB<sub>6</sub>, CeB<sub>6</sub>, and SrB<sub>6</sub>. Phys. Rev. B **57**, 8747 (1998).
  26. Süllo, S. et al. Metallization and magnetic order in EuB<sub>6</sub>. Phys. Rev. B **62**, 11626 (2000).
  27. Nie, S. et al. Magnetic Semimetals and Quantized Anomalous Hall Effect in EuB<sub>6</sub>. Phys. Rev. Lett. **124**, 076403 (2020).
  28. Gao, S. Y. et al. Time-Reversal Symmetry Breaking Driven Topological Phase Transition in EuB<sub>6</sub>. Phys. Rev. X **11**, 021016 (2021).
  29. Liu, W. L. et al. Spontaneous ferromagnetism induced topological phase transition in EuB<sub>6</sub>. arXiv:2103.04658.
  30. Süllo, S. et al. Structure and magnetic order of EuB<sub>6</sub>. Phys. Rev. B **57**, 5860 (1998).
  31. Brooks, M. L. et al. Magnetic phase separation in EuB<sub>6</sub> detected by muon spin rotation. Phys. Rev. B **70**, 020401(R) (2004).
  32. Cao, X. Y. et al. Giant nonlinear anomalous Hall effect induced by spin-dependent band structure evolution. arXiv:2103.09395.
  33. Kresse, G. et al. Efficiency of ab-initio total energy calculations for metals and semiconductors using a plane-wave basis set. Computational Materials Science **6**, 15 (1996).
  34. Kresse, G. et al. Electronic-structure-based chemical descriptors:(in) dependence on self-interaction and Hartree-Fock exchange. Phys. Rev. B **54**, 11169 (1996).
  35. Blochl, P. E. Projector augmented-wave method. Phys. Rev. B **50**, 17953 (1994).
  36. Kresse, G. et al. From ultrasoft pseudopotentials to the projector augmented-wave method. Phys. Rev. B **59**, 1758 (1999).
  37. Perdew, J. P. et al. Generalized Gradient Approximation Made Simple. Phys. Rev. Lett. **77**, 3865 (1996).
  38. Song, Z. D. et al. First principle calculation of the effective zeeman's couplings in topological materials. arXiv:1512.05084.